COMPARISON OF 3-D IMAGING ALGORITHMS FOR GROUND PENETRATING RADAR DATA

J. van der Kruk, C.P.A. Wapenaar, J.T. Fokkema
Section of Applied Geophysics, Faculty of Applied Earth Sciences, Delft University of Technology,
Mijnbouwstraat 120, 2628 RX Delft, The Netherlands
J.vanderKruk@ta.tudelft.nl, C.P.A.Wapenaar@ctg.tudelft.nl, J.T.Fokkema@ta.tudelft.nl

INTRODUCTION

The aim of an imaging procedure is to transform measured reflections to their true reflection position, by compensating for the propagation effects, resulting in a representation of the contrasting domain as accurate as possible. Several 3D imaging algorithms for Ground Penetrating Radar (GPR) data exist. Most of these imaging algorithms, like the one employing the Gazdag phase shift operator (Gazdag, 1978), are based on scalar seismic imaging algorithms. Another example of a scalar imaging algorithm is Synthetic Aperture Radar, SAR (Johansson and Mast, 1994), which was originally developed for remote sensing and is known in seismics as diffraction summation migration. However, it has advantages to take into account the vectorial character of the electromagnetic field and the radiation characteristics of the source and receiver antennas of a GPR system. Recently, such an imaging algorithm for GPR data has been developed (van der Kruk et al., 2000) and it employs 3-D multi-component data.
In this paper the imaging results using two scalar imaging operators − synthetic aperture radar (SAR) and Gazdag phase shift operator − are compared with results obtained with the multi-component imaging algorithm. We compare these algorithms by investigating the imaging results of the data of an elementary point scatterer in a homogeneous halfspace. This is representative for checking the adequacy of an imaging algorithm.

FORWARD MODEL

First we discuss the expression for the measured scattered electric field due to an elementary scatterer. Using the Born approximation, direct waves or multiples are assumed not to be present in the data. It is assumed that each point in the subsurface acts as an independent point scatterer producing only a single upwardly reflected signal. The electric field, measured at the acquisition surface $\mathbb{D}^{SR}$, is described by

$$\hat{E}^{\alpha\beta}(\boldsymbol{x}^R|\boldsymbol{x}^S,\omega) = \int\int\int_{\boldsymbol{x}^c\in\mathbb{D}^c} \chi(\boldsymbol{x}^c)\hat{\mathbf{G}}^{\alpha}(\boldsymbol{x}^R|\boldsymbol{x}^c,\omega)\cdot\hat{\mathbf{G}}^{\beta}(\boldsymbol{x}^c|\boldsymbol{x}^S,\omega)\hat{J}^{\beta}(\boldsymbol{x}^S,\omega)\mathrm{d}V, \qquad (1)$$

where $\mathbb{D}^c$ is the scattering domain and $\{\boldsymbol{x}^S,\boldsymbol{x}^R\}\in\mathbb{D}^{SR}$, where $x_3^S = x_3^R = 0$. α and β indicate the orientation of the receiver and the source, respectively, and have only a horizontal orientation, $\{\alpha,\beta\} = \{1,2\}$. This indicates that four different source and receiver combinations are possible. The configuration is depicted in Figure (1). $\hat{\mathbf{G}}^{\beta}(\boldsymbol{x}^c|\boldsymbol{x}^S,\omega)$ describes the propagation of the electric field, which is due to a point source $\hat{J}^{\beta}(\boldsymbol{x}^S,\omega)$ with spectrum $\hat{S}(\omega)$, to the location of the contrast $\chi(\boldsymbol{x}^c)$ at position $\boldsymbol{x}^c$. In case of a conductivity contrast, $\chi(\boldsymbol{x}^c)$ is real-valued; for a permittivity contrast it is purely imaginary. In both cases, this scatterer may be considered as a secondary source and the propagation from $\boldsymbol{x}^c$ towards the receiver is described by $\hat{\mathbf{G}}^{\alpha}(\boldsymbol{x}^R|\boldsymbol{x}^c,\omega)$. The scattered electric field

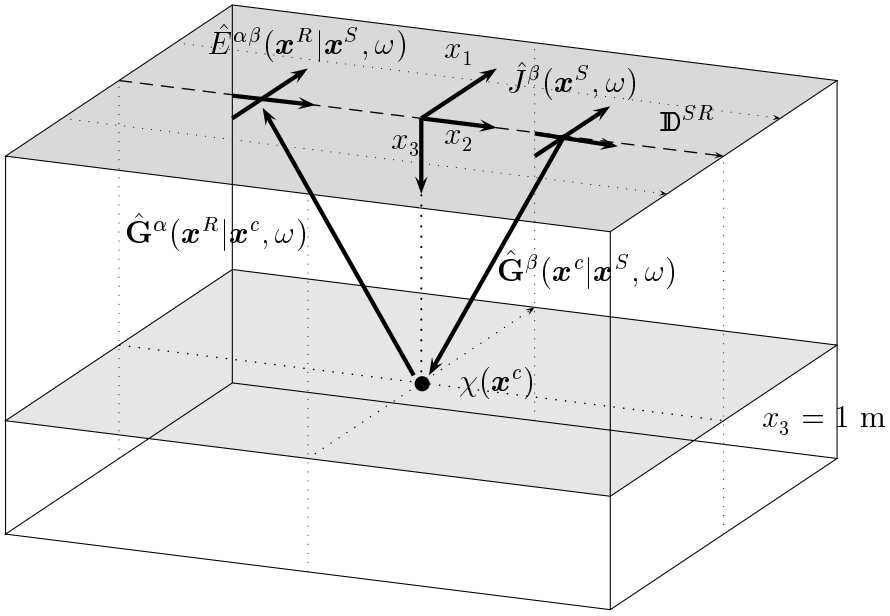

Figure 1: The configuration, with four possible source receiver setups.

$\hat{E}^{\alpha\beta}(\boldsymbol{x}^R|\boldsymbol{x}^S,\omega)$ is measured at position $\boldsymbol{x}^R$. Next, we assume that the source and receiver coordinates coincide (zero-offset), $\boldsymbol{x}^S = \boldsymbol{x}^R = \boldsymbol{x}^{ZO}$ and $x_3^{ZO} = 0$, resulting in

$$\hat{E}^{\alpha\beta}_{ZO}(\boldsymbol{x}^{ZO},\omega) = \int\int\int_{\boldsymbol{x}^c\in\mathbb{D}^c} \chi(\boldsymbol{x}^c)\hat{D}^{\alpha\beta}_{\mathbf{0}}(\boldsymbol{x}^{ZO}|\boldsymbol{x}^c,\omega)\hat{S}(\omega)\mathrm{d}V, \tag{2}$$

where $\hat{D}^{\alpha\beta}_{\mathbf{0}}(\boldsymbol{x}^{ZO}|\boldsymbol{x}^c,\omega)$ is the 3-D wave field extrapolator for zero offset, which is given by

$$\hat{D}^{\alpha\beta}_{\mathbf{0}}(\boldsymbol{x}^{ZO}|\boldsymbol{x}^c,\omega) = \hat{\mathbf{G}}^{\alpha}(\boldsymbol{x}^{ZO}|\boldsymbol{x}^c,\omega)\cdot\hat{\mathbf{G}}^{\beta}(\boldsymbol{x}^c|\boldsymbol{x}^{ZO},\omega), \tag{3}$$

$$= \hat{A}^{\alpha\beta}(\boldsymbol{x}^{ZO}|\boldsymbol{x}^c,\omega)\exp(-2j\omega|\boldsymbol{x}^{ZO}-\boldsymbol{x}^c|/c), \tag{4}$$

where c is the velocity of the electromagnetic waves in the lower halfspace. In Eq. (4) the scalar two-way wave extrapolator is written as a phase delay and a complex amplitude factor $\hat{A}^{\alpha\beta}(\boldsymbol{x}^{ZO}|\boldsymbol{x}^c,\omega)$.

IMAGING OPERATORS

In general form, an imaging algorithm can be written as

$$\chi^{\alpha\beta}_{image}(\boldsymbol{x}^i) = \int_\omega \frac{\mathrm{d}\omega}{\hat{S}(\omega)}\int\int_{\boldsymbol{x}^{ZO}\in\mathbb{D}^{SR}} \hat{D}^{\alpha\beta}_{image}(\boldsymbol{x}^i|\boldsymbol{x}^{ZO},\omega)\hat{E}^{\alpha\beta}_{ZO}(\boldsymbol{x}^{ZO},\omega)\mathrm{d}A, \tag{5}$$

and consists of two separate operations. The first is the inverse wave field extrapolation, which eliminates the propagation effects, and the second is the imaging procedure for which we sum the separate frequency components.
We will now focus on the inverse wave field extrapolator of the different imaging algorithms for one specific frequency. In this way the spatial resolution can be analysed. The SAR imaging operator is given by

$$\hat{D}^{\alpha\beta}_{image}(\boldsymbol{x}^i|\boldsymbol{x}^{ZO},\omega) = \exp(2j\omega|\boldsymbol{x}^i-\boldsymbol{x}^{ZO}|/c), \tag{6}$$

and compensates only for the phase delay (see also Eq. (4). The Gazdag phase shift method is actually carried out in the spatial Fourier domain, but effectively it means that the operator $\hat{D}^{\alpha\beta}_{image}$ contains a phase delay as well as an amplitude factor. Finally, note that for each source-receiver combination a separate image of the subsurface is obtained. The multi-component imaging algorithm uses for each source-receiver combination a different imaging operator $\hat{D}^{\alpha\beta}_{image}$. These operators are derived by a matrix inverse in the spatial Fourier domain, resulting in a stable approximate inverse operator, when two measured components due to one source are combined (van der Kruk et al., 2000),

$$\chi^{\beta}_{mc}(\boldsymbol{x}^i) = \sum_{\alpha=1}^{2} \chi^{\alpha\beta}_{image}(\boldsymbol{x}^i). \tag{7}$$

SYNTHETIC IMAGING RESULTS

The spatial resolution of a single point diffractor with a conductivity contrast at a depth of 1 meter in a dielectric halfspace is investigated. Full 3D downward extrapolation of the measured electric field to the depth level of the diffractor ($x^i_3 = 1$) is carried out for a frequency of $f = 500$ MHz. The relative permittivity of the lower halfspace is $\varepsilon_r = 4$ and the source function $\hat{S}(\omega)$ has unit amplitude. In Figures (2) - (4) the spatial resolution of 3-D downward extrapolation of full 3-D data is depicted for the multi-component and the two single component imaging operators for a depth of $x^i_3 = 1$ (see also Figure 1). The horizontal axes have been normalised with respect to the wavelength λ. The amplitudes are normalised to the maximum absolute value. Instead of a spatial delta function we observe a circular symmetric resolution function for the multi-component imaged contrast. The scalar imaging algorithms no longer show a circular symmetric resolution function and also show a non-zero imaginary imaged contrast. Note that a negative real contrast and a negative imaginary contrast is obtained using the SAR imaging algorithm and the Gazdag phase shift operator, respectively.

CONCLUSIONS

The multi-component imaging algorithm results in a circular symmetric resolution function if a point scatterer is imaged, whereas the scalar imaging algorithms show no circular symmetric resolution function. Moreover, for a conductivity contrast, the multi-component imaging algorithm correctly yields a real-valued contrast, whereas the scalar imaging algorithms yield both real and imaginary parts. These results show that the multi-component imaging algorithm results in a better representative imaged contrast. Further research has to be carried out to determine if we can distinguish between a permittivity and a conductivity contrast. The multi-component scheme seems to be best suited for this purpose. The next step is to compare the different imaging algorithms using experimental GPR data.

ACKNOWLEDGEMENTS

This research is supported by the Dutch Technology Foundation (STW).

REFERENCES

Gazdag, J., 1978, Wave equation migration with the phase-shift method, *Geophysics*, No. 43, pp. 1342-1351.

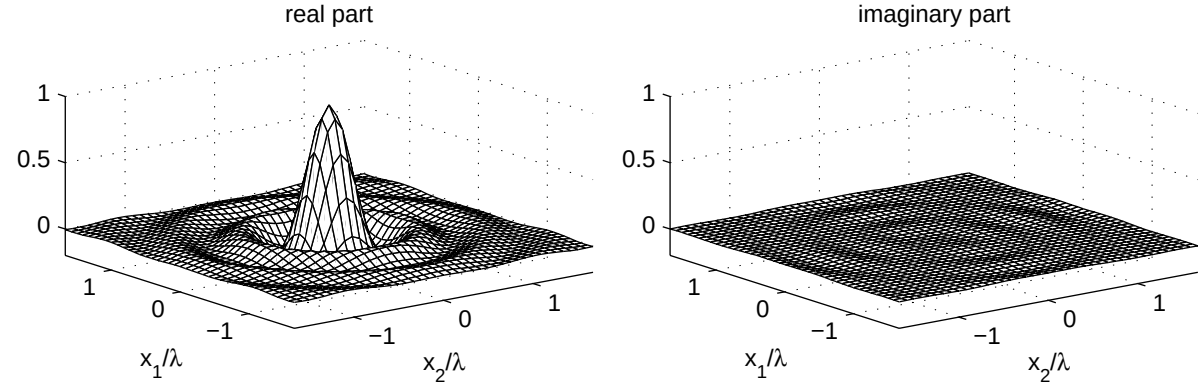

Figure 2: Real and imaginary parts of the imaged contrast for $f = 500$ MHz using the multi-component imaging algorithm.

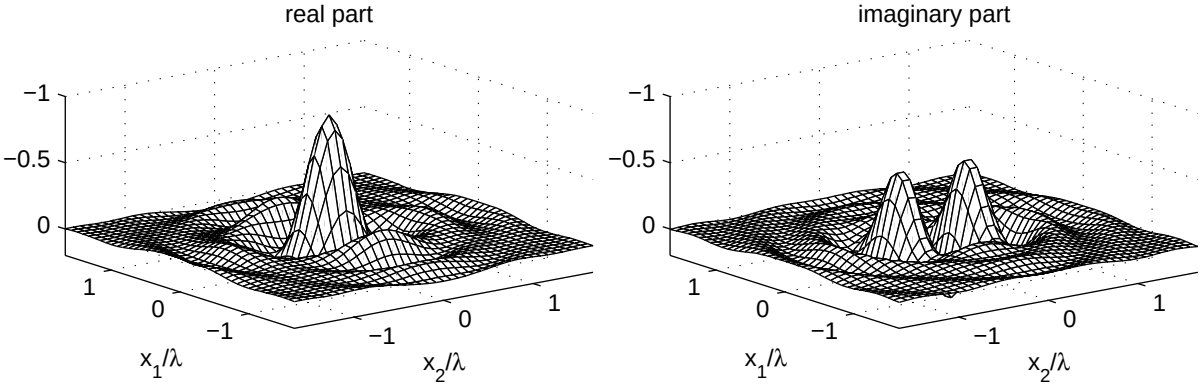

Figure 3: Real and imaginary parts of the imaged contrast for $f = 500$ MHz using the SAR imaging algorithm.

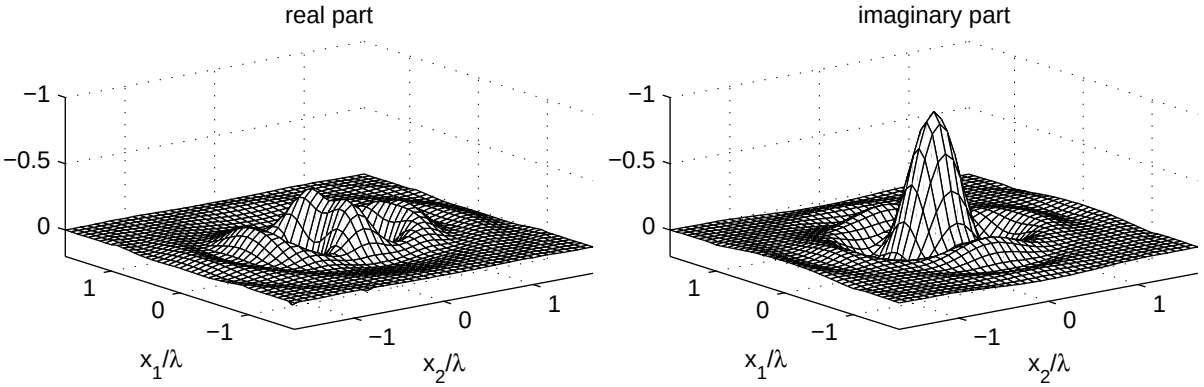

Figure 4: Real and imaginary parts of the imaged contrast for $f = 500$ MHz using the Gazdag imaging algorithm.

Johansson, E.M., Mast, J.E., 1994, Three-dimensional ground penetrating radar imaging using synthetic aperture time-domain focusing, *SPIE*, Vol. 2275, pp. 205-214.

van der Kruk, J., Wapenaar, C.P.A and Fokkema, J.T., 2000, Multi-component 3-D Imaging of ground penetrating radar data using matrix inversion in the spatial Fourier domain, *Proceedings Eighth international conference on Ground-Penetrating Radar*, Queensland, Australia, May 23-26, 2000.